

Autofocus Methods for Synthetic Aperture Radar Imaging

Chou-Wei Kiang

Department of Electrical Engineering, National Taiwan University

Email: b07611026@ntu.edu.tw

I. INTRODUCTION

Synthetic aperture radar (SAR) is a high-resolution, side-looking radar that is widely used in the area of remote sensing in recent decades. The SAR has versatile applications, including military or civilian surveillance, environment monitoring, and tracking of specific targets. There are several modes of SAR, such as strip-map SAR, spotlight SAR, and interferometric SAR (InSAR) [1].

One of the most commonly used mode is strip-map SAR. For strip-map SAR mode, the radar platform moves along a fixed direction with fixed speed, the radar would transmit and receive signals, which is usually a linear frequency modulated (LFM) signal, while radar is moving, and the antenna direction would be fixed, as demonstrated in the figure below. In this way, the received radar echoes over a number of transmitted signals are coherently collected and combined to obtain a received signal. The high-resolution imaging can then be formed by demodulate the received signal and apply proper imaging algorithms. The imaging process typically involves phase compensation of LFM signal in 1-D Fourier-transformed domain and 2-D frequency domain.

However, the SAR imaging can be blurred, or defocused, if the higher order phase is not well compensated. The phase error may be induced by unstable and irregular platform motion, propagation delay under different weather conditions, and the unknown target movement that is not in parallel with azimuth direction (platform moving direction) [2].

The focus of this term paper would be on investigating, comparing, and implementing several autofocus methods for SAR imaging. Two of the most popular autofocus methods including phase gradient autofocus (PGA) and minimum-entropy autofocus (MEA) would be investigated. The rest of the paper is organized as follows. The simple signal model, simulation scenario, and the basic concept of SAR autofocus would be introduced in Section II. Then, the phase gradient autofocus (PGA) would be investigated in Section III. The minimum-entropy autofocus and its variants would be introduced in Section IV. The matlab implementation and autofocused examples would be presented in Section V. Finally, some conclusions are drawn in Section VI.

II. BASIC SAR PRINCIPLES

A. Signal Modeling

First, the SAR signal model should be elaborated here. Assume the SAR platform moves in y direction with velocity

V_p . The point scatterers move with velocity $(v_x, v_y, 0)$. The n th scatterer is located at (x_n, y_n, z_n) at $\eta = 0$. The range between the SAR platform and the n th point scatterer is given by

$$R_n(\eta) = \sqrt{(x_n + v_x\eta)^2 + (y_n + v_y\eta - V_p\eta)^2 + (z_n - h_0)^2} \simeq R_{n0} + \alpha\eta + \beta\eta^2 \quad (1)$$

where the Taylor approximation is usually applied for the convenience of further signal processing, R_{n0} is the closest range, α is the coefficient of first order η , and β is the coefficient of second order η^2 .

A linear-frequency modulation (LFM) signal is usually used for SAR. The received signal after demodulation is given by

$$s_{rb}(\tau, \eta) = \sum_{n=1}^N A_n \text{rect}\left(\frac{\tau - 2R_n(\eta)/c}{T_r}\right) \text{rect}\left(\frac{\eta}{T_a}\right) e^{-j4\pi f_0 R_n(\eta)/c} e^{j\pi K_r(\tau - 2R_n(\eta)/c)^2} \quad (2)$$

where there are a total of N scatterers, τ is fast time along range direction and η is slow time along azimuth direction.

There are several conventional algorithms, including range-Doppler algorithm, chirp scaling algorithm, and ωK algorithm can be applied to focus the SAR signal in (2), the details can be found in [1]. By applying one of these conventional algorithms, the SAR image turn out to be

$$s_f(\tau, \eta) = \sum_{n=1}^N c_n A_n e^{-j4\pi f_0 R_{n0}/c} \text{sinc}\left\{B_r\left(\tau - \frac{2R_{n0}}{c}\right)\right\} \text{sinc}(B_a\eta) \quad (3)$$

where c_n is the constant arouses during the imaging process, the sinc function in τ indicates focus in the range direction, and the sinc function in η indicates focus in the azimuth direction.

B. Simulation Scenario

Assume the image is obtained from an X-band SAR with center frequency $f_0 = 10$ GHz, and the radar platform velocity is $V_p = 200$ m/s, while all the point targets are moving with $v_y = -100$ m/s, and let the spacing of point targets be $\Delta x = 5$ m along x -direction, $\Delta y = 5$ m along y -direction on the ground. Fig.1(a) shows the magnitude of SAR image after RDA is applied when $v_x = 0$ m/s, in which the point targets are well focused in (τ, η) time domain. Fig.1(b) shows the

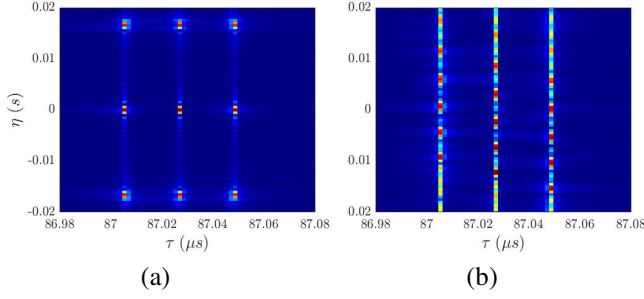


Fig. 1. Magnitude of SAR image after applying conventional RDA, with (a) $v_x = 0$ m/s, (b) $v_x = 100$ m/s, and $\Delta x = \Delta y = 5$ m.

magnitude of SAR image after RDA is applied when $v_x = 100$ m/s, in which the point targets are blurred along η -domain when the points targets have movement along x -direction. If the autofocus can be successfully applied, the point targets in Fig.1(b) should be focused similar as in Fig.1(a).

C. SAR Autofocus

The autofocus methods can be generally categorized based on two features. First, the autofocus methods can be magnitude-based or phase-based. Second, the autofocus methods can be categorized into parametric or non-parametric [1]. When magnitude-based method is applied, the parameters used to evaluate the blurriness or the sharpness of an image is based on the magnitude or intensity of an image. As for the phase-based method, the parameters used for evaluation is based on the phase of an image. The parametric methods assume the phase error is a polynomial of azimuth time η or a polynomial of azimuth frequency f_η . The order of the polynomial in parametric methods can be pre-determined by the operator, or can be determined according to the size of phase error induced by different order with adaptive methods. The advantage of parametric method is that the phase error can be modeled into simple form, the autofocusing problem is simplified as optimization problem to determine polynomial coefficients, which is more computationally efficient.

Nevertheless, the relative motion between the SAR platform and the target is not always steady and ideal, there may be unexpected motions such as SAR platform perturbation and the target might be with rotational and vibrational motion, leading to irregular and unpredictable form of phase error. The noise and the attenuation due to propagation in air in field test may also induced different form of phase error. Thus, the non-parametric methods assume that the phase error is irregular, which bears no general mathematical form, which can be applied more generally under different environment. Nevertheless, non-parametric methods usually fit the phase error by solving the optimization problem with trial-and-error, which may be time consuming and inefficient [2]. If the noise is presented and the signal-to-noise ratio (SNR) is not large enough, the parametric method may not perform well since the induced error cannot be well-matched with polynomial. Thus, it is speculated that the non-parametric autofocus methods should results in a better-focused SAR image when the noise is considered.

III. PHASE GRADIENT AUTOFOCUS

Phase gradient autofocus (PGA) is the state-of-the-art algorithm for SAR autofocus. Nevertheless, the earliest developed PGA can only be applied to spotlight SAR, instead of strip-map SAR, which is the most common operation mode of SAR. Thus, some modifications have to be made when applying PGA to strip-map SAR images [3].

Phase gradient autofocus (PGA) is a non-parametric autofocus method, which is able to deal with unpredictable perturbations to the phases of received signal. That is, if the image is still blurred after all available motion compensation are done for known platform motions or target motions, PGA is capable of further focusing to obtain a SAR image with better quality, enabling us to better identify targets. The basic concept of PGA is to approximately estimate the gradient, or the derivative, of the unwanted phase error with the given blurred complex SAR image solely [4]. In other words, the SAR imaging process of obtaining blurred SAR image in (3) from the received signal in (2) need not to be known when applying PGA.

A. PGA for Spotlight SAR [4]

The implementation of PGA can be summarized into four important steps, which are center shifting, windowing, estimation of phase gradient, and iterative correction [4]. For spotlight SAR, the range-compressed phase-history $S_f(\tau, f_\eta)$ is related to the range-compressed complex SAR imaging $s_f(\tau, \eta)$ (3) by [5]

$$s_f(\tau, \eta) = \mathcal{F}_\eta^{-1} \{S_f(\tau, f_\eta)\} = \int_{-\infty}^{\infty} S_f(\tau, f_\eta) e^{j2\pi f_\eta \eta} df_\eta \quad (4)$$

where range compression is the inverse range Fourier transform for spotlight SAR.

The magnitude and phase of the range-compressed phase-history domain data $S_f(\tau, f_\eta)$ of τ -th range line can be separately written as [6]

$$S_{f,\tau}(f_\eta) = |S_{f,\tau}(f_\eta)| \exp\{j[\phi_\tau(f_\eta) + \phi_e(f_\eta)]\} + n(f_\eta) \quad (5)$$

where $|S_{f,\tau}(f_\eta)|$ and $\phi_\tau(f_\eta)$ are magnitude and phase of the τ -th range line, respectively, $\phi_e(f_\eta)$ is the uncompensated phase error, which is the same across all range lines for spotlight SAR, and $n(f_\eta)$ is the additive speckle noise. The different range lines of phase-history domain data are separately considered and processed is because the phase error of SAR image usually occurs across azimuth direction after proper range compression, resulting in defocused image along azimuth direction only.

1) *Center Shifting (Circular Shifting)*: By taking the inverse azimuth Fourier transform of $S_{f,\tau}(f_\eta)$, we have

$$s_{f,\tau}(\eta) = \mathcal{F}_\eta^{-1} \{S_{f,\tau}(f_\eta)\} \quad (6)$$

which is the complex SAR imaging in (3). In order to remove the frequency offset induced by Doppler effect, the strongest scatterer of each range line in $S_{f,\tau}(f_\eta)$ in (6) should be shifted to the center of the image. In practice, the center shifting can be achieved by circular shifting the strongest scatterer of each range line in the discrete data to the center of the range

line. By center shifting, the strongest scatterers in each range line are well aligned, so the signal-to-noise ratio (SNR) can be significantly improved such that the phase error estimated with higher accuracy. Also, after center shifting is done, the windowing can be more easily applied later.

2) *Windowing*: After center shifting is done, the windowing can then be applied to preserve the majority of the dominant blur, while the data with small energy that is not helpful for phase error estimation, are filtered out. In this way, the signal-to-interference-plus-noise ratio (SINR) of the data can be effectively improved [7].

The choice of the window width is the crucial part of this step. It is mentioned earlier that the unwanted phase error $\phi_e(f_\eta)$ should be the same across all range lines for spotlight SAR. Thus, after the strongest scatterers of each range line are aligned in the previous step, let $s_{g,\tau}(\eta)$ be the center shifted version of $s_{f,\tau}(\eta)$, then a one-dimensional intensity function

$$I(\eta) = \sum_{\tau} |s_{g,\tau}(\eta)|^2 \quad (7)$$

can be obtained by incoherently sum over all the range bins, since the phase error across all ranges are the same. Typically the window is chosen to cutoff at the intensity where the intensity function is 10 dB lower from the peak. In other words, at $\eta = \eta'$, the $I(\eta')$ is 10 dB lower from the peak, then a threshold can be applied such that the $I(\eta) = 0$ for $\eta > \eta'$, and in this case, the width of window is $W = 2\eta'$.

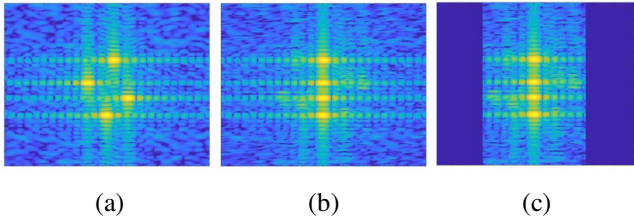


Fig. 2. The magnitude of (a) $s_f(\tau, \eta)$, (b) $s_g(\tau, \eta)$, (c) $s'_g(\tau, \eta)$ [7]. The vertical axis of these three figures is range (τ -axis) and the horizontal axis is azimuth (η -axis).

3) *Phase Gradient Estimation*: Let $s'_{g,\tau}(\eta)$ be the signal after the center shifting and windowing are both applied. Then, by taking azimuth Fourier transform of $s'_{g,\tau}(\eta)$, we have

$$\begin{aligned} S'_{g,\tau}(f_\eta) &= |S'_{g,\tau}(f_\eta)| e^{j[\phi_\tau(f_\eta) + \phi_e(f_\eta) + \theta_\tau(f_\eta)]} \\ &\quad + n(f_\eta) e^{j\theta_\tau(f_\eta)} \\ &= |S'_{g,\tau}(f_\eta)| e^{j[\phi_\tau(f_\eta) + \phi_e(f_\eta) + \theta_\tau(f_\eta)]} \\ &\quad + \alpha(f_\eta) e^{j\theta_n(f_\eta)} e^{j\theta_\tau(f_\eta)} \end{aligned} \quad (8)$$

where $n(f_\eta) = \alpha(f_\eta) e^{j\phi_n(f_\eta)}$ is the assumed additive noise distribution, and $\theta_\tau(f_\eta)$ is the scatterer-dependent phase induced by center shifting. The signal $S'_{g,\tau}(f_\eta)$ can be further rewritten as

$$S'_{g,\tau}(f_\eta) = |S'_{g,\tau}(f_\eta)| e^{j\phi_e(f_\eta)} e^{j[\phi_\tau(f_\eta) + \theta_\tau(f_\eta)]} \left[1 + \frac{\alpha(f_\eta)}{|S'_{g,\tau}(f_\eta)| e^{j\phi_\tau(f_\eta)}} e^{j[\phi_n(f_\eta) - \phi_e(f_\eta)]} \right] \quad (9)$$

The phase of $S'_{g,\tau}(f_\eta)$ can then be extracted as [6]

$$\begin{aligned} \phi(f_\eta) &= \angle S'_{g,\tau}(f_\eta) = \phi_e(f_\eta) + \\ &\quad \tan^{-1} \left[\frac{\frac{\alpha(f_\eta)}{|S'_{g,\tau}(f_\eta)|} \text{Im} \{ e^{j[\phi_n(f_\eta) - \phi_e(f_\eta) - \phi_\tau(f_\eta)]} \}}{1 + \frac{\alpha(f_\eta)}{|S'_{g,\tau}(f_\eta)|} \text{Re} \{ e^{j[\phi_n(f_\eta) - \phi_e(f_\eta) - \phi_\tau(f_\eta)]} \}} \right] \\ &\simeq \phi_e(f_\eta) + \frac{\alpha(f_\eta)}{|S'_{g,\tau}(f_\eta)|} \text{Im} \{ e^{j[\phi_n(f_\eta) - \phi_e(f_\eta) - \phi_\tau(f_\eta)]} \} \\ &= \phi_e(f_\eta) + V_\tau(f_\eta) \end{aligned} \quad (10)$$

where the signal-to-noise ratio (SNR) is assumed to be large such that $\alpha(f_\eta) \ll |S'_{g,\tau}(f_\eta)|$.

For a complex signal $f(t) = |f(t)| e^{j\phi(t)}$, the instantaneous phase derivative can be derived as

$$\begin{aligned} \dot{\phi}(t) &= \frac{d\phi(t)}{dt} = \frac{d}{dt} \tan^{-1} \left(\frac{\text{Im}\{f(t)\}}{\text{Re}\{f(t)\}} \right) \\ &= \frac{1}{1 + \left(\frac{\text{Im}\{f(t)\}}{\text{Re}\{f(t)\}} \right)^2} \frac{d}{dt} \left(\frac{\text{Im}\{f(t)\}}{\text{Re}\{f(t)\}} \right) \\ &= \frac{\text{Re}\{f(t)\} \frac{d\text{Im}\{f(t)\}}{dt} - \text{Im}\{f(t)\} \frac{d\text{Re}\{f(t)\}}{dt}}{\left[1 + \left(\frac{\text{Im}\{f(t)\}}{\text{Re}\{f(t)\}} \right)^2 \right] \text{Re}\{f(t)\}^2} \\ &= \frac{\text{Im}\{\dot{f}(t) f^*(t)\}}{|f(t)|^2} \end{aligned} \quad (11)$$

Thus, a linear unbiased minimum variance (LUMV) estimator of signal $S'_{g,\tau}(f_\eta)$ in (9) can be defined as [4], [6]

$$\begin{aligned} \hat{\phi}_{\text{lumv}}(f_\eta) &= \frac{\sum_{\tau} \text{Im}\{S'_{g,\tau}(f_\eta)^* \dot{S}'_{g,\tau}(f_\eta)\}}{\sum_{\tau} |S'_{g,\tau}(f_\eta)|^2} \\ &\simeq \dot{\phi}_e(f_\eta) + \frac{\sum_{\tau} |S'_{g,\tau}(f_\eta)|^2 \dot{V}_\tau(f_\eta)}{\sum_{\tau} |S'_{g,\tau}(f_\eta)|^2} \end{aligned} \quad (12)$$

which is used to estimate the gradient of phase error $\dot{\phi}_e(f_\eta)$, where the operator $\dot{\cdot}$ indicates gradient or derivative of a variable. From (12), the LUMV estimator yields the gradient of the unwanted phase error $\phi_e(f_\eta)$, with an extra error term that is relatively small.

Apart from the LUMV estimator, other estimators such as Knox-Thompson kernel [4], maximum likelihood (ML) estimator [8], and weighted maximum likelihood (WML) estimator [9] can also be used to replace the LUMV estimator.

4) *Iterative Phase Correction*: With the estimated phase gradient in (12), the estimated phase error is

$$\hat{\phi}_e(f_\eta) \simeq \int_{f_{\eta_0}}^{f_\eta} \hat{\phi}_{\text{lumv}}(f'_\eta) df'_\eta \quad (13)$$

which is the cumulation sum of $\hat{\phi}_{\text{lumv}}(f_\eta)$ along f_η -axis, and f_{η_0} is the minimum azimuth frequency of the given SAR image data. Then, the phase error in $S'_{g,\tau}(f_\eta)$ can be compensated as

$$S''_{g,\tau}(f_\eta) = S'_{g,\tau}(f_\eta) e^{-\hat{\phi}_e(f_\eta)} \quad (14)$$

Finally, by taking the inverse azimuth Fourier transform of $S''_{g,\tau}(\eta)$, we have

$$s''_{g,\tau}(\eta) = \mathcal{F}_\eta^{-1} \{ S''_{g,\tau}(f_\eta) \} \quad (15)$$

which is the resulting signal after the first iteration of PGA is accomplished.

The PGA should be iteratively applied furthermore. After each iteration, the estimation and correction of phase error should result in a more focused image. When the image becomes more focused, the SCR can be improved, and then the center shifting can be achieved with higher precision. Finally, the PGA would converge after several iterations, and the obtained image should be focused with higher quality [4].

B. Strip-map PGA Modifications [3], [10], [11]

In strip-map SAR mode, the antenna point direction is fixed, as shown in Fig.3(a), with a fixed platform speed, the antenna beam would sweep through a stripe area at a fixed rate. As for the spotlight SAR mode, the antenna direction can be steered such that the antenna beam is always focused to a certain area of interest, as demonstrated in Fig.3(b). In this way, the resolution of SAR image can be improved due to the increasing information from different angle of the same target area [1].

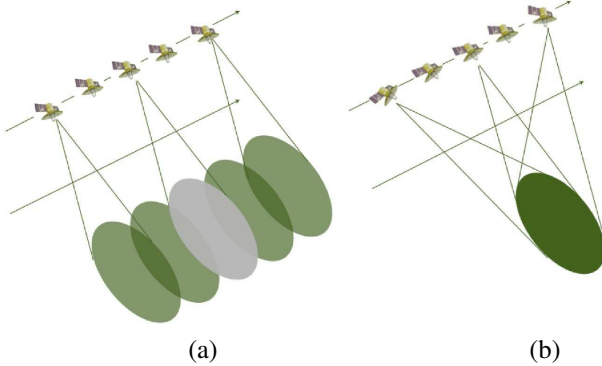


Fig. 3. The operation schematic of (a) strip-map SAR, (b) spotlight SAR [12].

For a spotlight SAR image, a target in the area of interest is always illuminated by the antenna beam throughout a single flight. Nevertheless, for a strip-map SAR image, each target is only illuminated by the antenna beam for a limited time during a single flight. Each single scatterer in strip-map SAR image is formed from a part of certain linear FM chirp signal, so the phase error cannot be aligned in range-compressed domain with only center shifting and center shifting.

In spotlight mode, the process of received signal is relatively simple. After range compression and motion compensation, the PGA can then be directly applied to autofocus the image. Nevertheless, in strip-map mode, the chirp deconvolution is required to disperse the phase of each scatterer to the correct azimuth grid in each range line [11]. In this way, the phase of each range line can be directly summed to obtain a one-dimensional intensity function as in (7). But if the conventional algorithms for strip-map SAR imaging such as range Doppler algorithm (RDA) is used, the chirp deconvolution along azimuth domain is already accomplished in azimuth compression step.

Therefore, only an extra step of subaperture dividing is required before applying conventional PGA to strip-map SAR

image. The apertures of individual scatterer do not coincide exactly for strip-map SAR image since the antenna point direction is fixed. Thus, if PGA is directly applied to the whole strip-map SAR image, the phase error cannot be precisely compensated. The best way to deal with this problem is to divide the SAR image along azimuth domain such that the length of each subaperture is about one-third to two-thirds of the total synthetic aperture length. The concept of subaperture dividing is shown in Fig.4. Note that the subapertures can be overlapped with each other to avoid the discontinuity when the resulting image after PGA are stitched together.

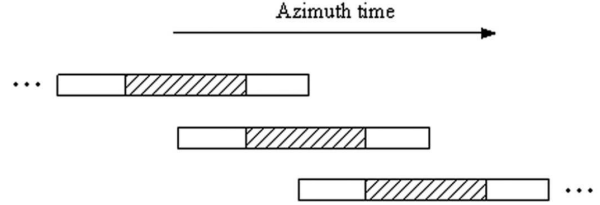


Fig. 4. The concept of subaperture dividing [3].

IV. MINIMUM-ENTROPY AUTOFOCUS

The minimum-entropy autofocus (MEA) is a magnitude-based method. The image entropy is used to evaluate the sharpness of an image, which is calculated based on the magnitude, or intensity, of the given image. There are several variants of minimum-entropy method, some of which are parametric methods, while others are non-parametric methods.

In this section, three variants of parametric MEA will be introduced. The first one is the parametric MEA with simple polynomial model, which models the phase error as a simple polynomial, and the autofocus can be accomplished by determining coefficients of polynomial to minimize the image entropy. The second variant is the parametric MEA with adaptive-order polynomial model, which is the modified version of parametric MEA with simple polynomial model. The last one is a non-parametric MEA, which should be able to handle phase error of any form.

If the moving target with motion not in parallel with the SAR platform movement will induce higher order phase error, resulting in the blurring in the final SAR image [10]. This may be due to the fact that the range model in (1) is only approximated to the second order of η , the higher order phase error that is not well compensated may be passed down to the final SAR image. Therefore, autofocus can be applied to improve the quality of SAR image to better identify the point targets. A parametric minimum-entropy method with adaptive-order polynomial model is proposed in [2] to achieve autofocus and enhance the image quality.

Assume the phase error of SAR signal $s_f(\tau, \eta)$ in (3) can be modeled as $\varphi(f_\eta)$ in azimuth frequency domain. This is a reasonable assumption, since the blurriness in the SAR image can be thought of as magnitude of some signal components are time-shifted from the correct position along η -domain, and the time-shifting in η -domain is the phase delay in f_η -domain.

The azimuth Fourier transform of $s_f(\tau, \eta)$ in (3) can be defined as

$$S_f(\tau, f_\eta) = \mathcal{F}_\eta \{s_f(\tau, \eta)\} = \int_{-\infty}^{\infty} s_f(\tau, \eta) e^{-j2\pi f_\eta \eta} d\eta \quad (16)$$

A phase compensation term $e^{-j\varphi(f_\eta)}$ can then be multiplied with $S_f(\tau, f_\eta)$ to obtain

$$S'_f(\tau, f_\eta) = S_f(\tau, f_\eta) e^{-j\varphi(f_\eta)} \quad (17)$$

which can be inverse azimuth Fourier transformed to have

$$s'_f(\tau, \eta) = \mathcal{F}_\eta^{-1} \{S'_f(\tau, f_\eta)\} \quad (18)$$

which should give a well-focused SAR image $|s'_f(\tau, \eta)|$ if the phase error is well determined. Different approaches are used to estimate phase error $\varphi(f_\eta)$ in different autofocus methods.

The entropy of SAR image $s'_f(\tau, \eta)$ can be defined as [2]

$$\begin{aligned} S_{\text{image}}(s'_f) &= \sum_{n=1}^{N_a} \sum_{m=1}^{N_r} \frac{|s'_f[m, n]|^2}{I_{\text{tot}}} \ln \frac{I_{\text{tot}}}{|s'_f[m, n]|^2} \\ &= \ln I_{\text{tot}} - \frac{1}{I_{\text{tot}}} \sum_{n=1}^{N_a} \sum_{m=1}^{N_r} |s'_f[m, n]|^2 \ln |s'_f[m, n]|^2 \end{aligned} \quad (19)$$

where

$$I_{\text{tot}} = \sum_{n=1}^{N_a} \sum_{m=1}^{N_r} |s'_f[m, n]|^2 \quad (20)$$

is the total intensity of image, and the SAR image data in $s'_f(\tau, \eta)$ is sampled as $s'_f[m, n]$, where $1 \leq m \leq N_r$ and $1 \leq n \leq N_a$. The intuition of minimum entropy method is that entropy can be used to evaluate the sharpness of a given image. When an image is blurred by the phase error $\varphi(f_\eta)$, the sharpness of the image decreases. Thus, MFA aims to estimate the proper $\varphi(f_\eta)$ such that the entropy of $s'_f(\tau, \eta)$ is minimized. In this way, the SAR image with maximum sharpness and minimum blurriness can be obtained.

A. Parametric MEA with Conventional Polynomial Model

The phase error can be modeled by simple polynomial as

$$\varphi(f_\eta) = \sum_{p=2}^P \varphi_p(f_\eta) = \sum_{p=2}^P \beta_p f_\eta^p \quad (21)$$

where β_p is the coefficient of p th order, and P is the maximum order that should be determined by operator. Note that the zeroth-order and first-order terms are neglected since both of them have no effect on entropy and the first-order term would only result in shift along azimuth domain [2].

The intuition of this method is to get a sharper image $s'_f(\tau, \eta)$ from $s_f(\tau, \eta)$ by tuning the coefficient β_p for each of p th order in $\varphi(f_\eta)$ such that the image entropy of $s'_f(\tau, \eta)$.

The minimum entropy criterion is used to form an optimization problem as

$$\tilde{\beta} = \arg \min_{\tilde{\beta}} S_{\text{image}}(s'_f(\tau, \eta)) \quad (22)$$

where $\tilde{\beta} = [\tilde{\beta}_2, \tilde{\beta}_3, \dots, \tilde{\beta}_P]$ is the estimated coefficient vector.

B. Parametric MEA with Adaptive-order Polynomial Model [2]

In [2], the phase error $\varphi(\omega)$ can be modeled as an adaptive-order polynomial as

$$\varphi(\omega) = \sum_{p=2}^P \varphi_p(\omega) = - \sum_{p=2}^P \frac{\pi \beta_p}{p} \left(\frac{\omega - \omega_0}{\pi} \right)^p, \quad \text{for } |\omega - \omega_0| \leq \pi \quad (23)$$

where β_p is the coefficient to be determined, $\omega = 2\pi f_\eta$, and $\omega_0 = 2\pi f_{\eta 0}$ is the Doppler centroid frequency in radians. The definition of $\varphi(\omega)$ is restricted to $|\omega - \omega_0| \leq \pi$, since angular frequency ω is periodic with period 2π . Note that both zeroth and first order terms are omitted in (23) since the both of zeroth and first order terms have no effects on image entropy, and the first-order term is only related to shift in azimuth domain.

Mathematically, the theoretical β_p can be calculated for each p . The p th order phase error $\varphi(\omega)$ in (23) would result in a group delay

$$\Delta_p(\omega) = - \frac{d\varphi_p(\omega)}{d\omega} = \beta_p \left(\frac{\omega - \omega_0}{\pi} \right)^{p-1} \quad (24)$$

which is the time delay at ω due to the p th order phase error. Then, by taking the limit of (24), the coefficient β_p can be determined as

$$\beta_p = \lim_{\omega \rightarrow (\omega_0 + \pi)^-} \Delta_p(\omega) = \lim_{\omega \rightarrow (\omega_0 + \pi)^-} \beta_p \left(\frac{\omega - \omega_0}{\pi} \right)^{p-1} \quad (25)$$

The relationship between coefficient β_p in (25) and group delay $\Delta_p(\omega)$ in (24) is demonstrated in Fig.5.

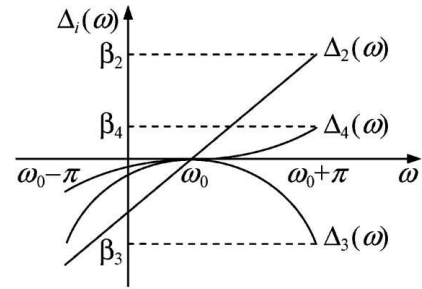


Fig. 5. Illustration of relationship between coefficient β_p and group delay $\Delta_p(\omega)$ [2].

In practice, it is difficult to perform differentiation on numerical data, and if the SAR image is focused with different algorithm, the estimated $\tilde{\beta}_p$ should vary slightly. Thus, a reasonable initial guess should be first determined, then each of the p th order coefficient can be estimated by iteratively searching for the $\tilde{\beta}_p$ such that the image entropy $S_{\text{image}}(s'_f(\tau, \eta))$ is minimized. In other words, the coefficients can be estimated by solving the optimization problem

$$\tilde{\beta} = \arg \min_{\tilde{\beta}} S_{\text{image}}(s'_f(\tau, \eta)) \quad (26)$$

which is similar as in Section IV-B, but with different polynomial model, where $\tilde{\beta} = [\tilde{\beta}_2, \tilde{\beta}_3, \dots, \tilde{\beta}_P]$ is the estimated coefficient vector. The maximum order P can be determined

adaptively such that the program stops execution when $\tilde{\beta}_p \simeq 0$ for both order $p = P - 1$ and $p = P$.

C. Non-parametric MEA [13], [14]

Non-parametric MEA is also an iterative autofocus method similar to PGA. In [13], an iterative stage-by-stage approaching (SSA) algorithm is proposed to determine phase error based on entropy minimization of a 2-D image. The SSA searches for optimum with downhill searching technique, in which the phase gradient is not required to be calculated. In the first iteration, a large enough searching step Δ_1 is manually chosen, then the step Δ_i decreases stage-by-stage, that is, the step decreases as the number of iteration increases.

Unlike the aforementioned parametric MEA, there are no restrictions on the form of phase error, the phase error can be polynomial of any order, or any other form, even random.

Assume that the SAR image has number of range lines N_r and number of samples per range line N_a , then we can let $S_f[m, n]$ be the sampled version of $S_f(\tau, f_\eta)$ in (16), where $1 \leq m \leq N_r$ and $1 \leq n \leq N_a$. Denote $\hat{\varphi}_{e,i,m}[n]$ as the sampled version of estimated phase error $\varphi(f_\eta)$ of the m -th range line in the i -th iteration.

The SSA can be accomplished with the following steps:

1. Initialize needed parameters. Set iteration number $i = 1$, step size $\Delta_1 = \pi$, estimated phase error vector $\hat{\varphi}_{e,1,1} = \hat{\varphi}_{e,1,N_r} = 0_{N_a \times 1}$ as a null vector of size $N_a \times 1$.
2. In the current i -th iteration, the estimated phase error vector can be evaluated range line by range line.
3. For the m -th range line, there are three possible choices of phase error vector, which are

$$\varphi_1 = \hat{\varphi}_{e,i,m-1} \quad (27)$$

$$\varphi_2 = \hat{\varphi}_{e,i,m-1} + [0, \dots, 0, \Delta_i, 0, \dots, 0]_{1 \times N_a}^T \quad (28)$$

$$\varphi_3 = \hat{\varphi}_{e,i,m-1} + [0, \dots, 0, -\Delta_i, 0, \dots, 0]_{1 \times N_a}^T \quad (29)$$

where the term Δ_i is the m -th element in the vector in (28), and the term $-\Delta_i$ is the m -th element in the vector in (29).

4. The final choice among these three vectors can be determined according to

$$\begin{aligned} \hat{\varphi}_{e,i,m} &= \arg \min_{\varphi_p} S_{\text{image}}(\mathcal{F}_\eta^{-1}\{S_f e^{-j\varphi_p}\}) \\ &= \arg \min_{\varphi_p} H(\varphi_p), \quad p = 1, 2, 3 \end{aligned} \quad (30)$$

where the image entropy S_{image} is defined in (19).

5. Repeat steps 3 and 4 from $m = 2$ to N_r to accomplish a single iteration.
6. After the i -th iteration, define a cost function

$$C_i = \left| \frac{H(\hat{\varphi}_{e,i,1}) - H(\hat{\varphi}_{e,i,N_r})}{H(\hat{\varphi}_{e,i,1})} \right| \quad (31)$$

where $H(\varphi) = S_{\text{image}}(\mathcal{F}_\eta^{-1}\{S_f e^{-j\varphi}\})$ as defined in (30). If $C_i > T_0$, where T_0 is a preset threshold, then it is implied that the change of estimated phase vector is obvious after one complete iteration. Thus, update $\hat{\varphi}_{e,i,1} = \hat{\varphi}_{e,i,N_r}$, then repeat the same iteration again, starting from step 2.

Otherwise, if $C_i \leq T_0$, then we can proceed to the next step.

7. Define another cost functions between two iterations as

$$D_i = \left| \frac{H(\hat{\varphi}_{e,i-1,N_r}) - H(\hat{\varphi}_{e,i,N_r})}{H(\hat{\varphi}_{e,i-1,N_r})} \right| \quad (32)$$

If $D_i > T_1$, where T_1 is another preset threshold, then the change between two iterations are significant. Thus, we can proceed to the next iteration, that is, update the iteration as $i = i + 1$, update the step size as $\Delta_i = \Delta_i / 2$, update the estimated phase vector $\hat{\varphi}_e = \hat{\varphi}_{e,i-1,N_r}$, then start from step 2 again.

Otherwise, if $D_i \leq T_1$, the resulting estimated phase vector is determined as $\hat{\varphi}_e = \hat{\varphi}_{e,i,N_r}$, and the SSA execution can be terminated.

The SSA processes through all range lines since if the SAR image signal is properly aligned and center shifted as in PGA, the phase error should be the same across all range lines. So after the first iteration, the estimated phase vector $\hat{\varphi}_e = \hat{\varphi}_{e,1,N_r}$ would be only consists of 0, $-\pi$, π . In the further iterations, each value in $\hat{\varphi}_{e,i,N_r}$ would be adjusted with smaller step according to the minimum entropy criteria. The estimated error will converge at some point, and by compensating the phase error according to (17) and (18), the autofocus is completed and a well-focused SAR image should be obtained.

V. MATLAB IMPLEMENTATION AND DISCUSSIONS

There are three sets of simulated point targets SAR image data with different spacing Δ_x, Δ_y , which are attached in the compressed file, and can be loaded with the main function written in 'SAR_autofocus_v4.m'. In addition, there are two sets of real SAR image data also attached in the compressed file, and can be loaded with the main function written in 'SAR_autofocus_v4.m'. One of the real SAR image data is the original version downloaded from [15], while some noise is added to original data to obtain another set of real SAR image data.

A. Phase Gradient Autofocus (PGA)

The implementation Matlab code of PGA is modified from [16]. The function of PGA is written in 'pga_v2.m', which can be executed from the main function written in 'SAR_autofocus_v4.m'.

The image entropy S_{image} defined in (19) for MEA can be once again used to evaluate the effectiveness of PGA. If PGA is successfully applied, the resulting image should be more well-focused, indicating larger sharpness, and thus indicating smaller image entropy.

B. Minimum-Entropy Autofocus (MEA)

The implementation Matlab code of parametric MEA is all written by myself. In this section, the parametric MEA with conventional polynomial model would be implemented. The

maximum order of the polynomial will be pre-determined as $P = 3$ and fixed for the simplicity of simulation, that is

$$\varphi(f_\eta) = \sum_{p=2}^3 \varphi_p(f_\eta) = \beta_2 f_\eta^2 + \beta_3 f_\eta^3 \quad (33)$$

In practice, the implementation of MEA requires a complex multiplication and an IFT for each guess of (β_2, β_3) , thus, a proper image size should be first determined to avoid heavy computational burden.

In the simulation, the coefficients β_2 and β_3 are determined by first setup a 2-D searching grid, then calculate the respective image entropy after compensating the phase error with each set of (β_2, β_3) on 2-D grid. This is a simple and straightforward method, but it may be time consuming. The efficiency can be further improved by evaluating the coefficients with other optimization methods such as convex optimization.

C. 9-point Targets

If the spacing of the point targets along x , y -directions, the effectiveness of MEA may be different. Thus, three different scenarios are designed, which are

1. $\Delta x = \Delta y = 5$ m
2. $\Delta x = 4$ m, $\Delta y = 10$ m
3. $\Delta x = 10$ m, $\Delta y = 4$ m.

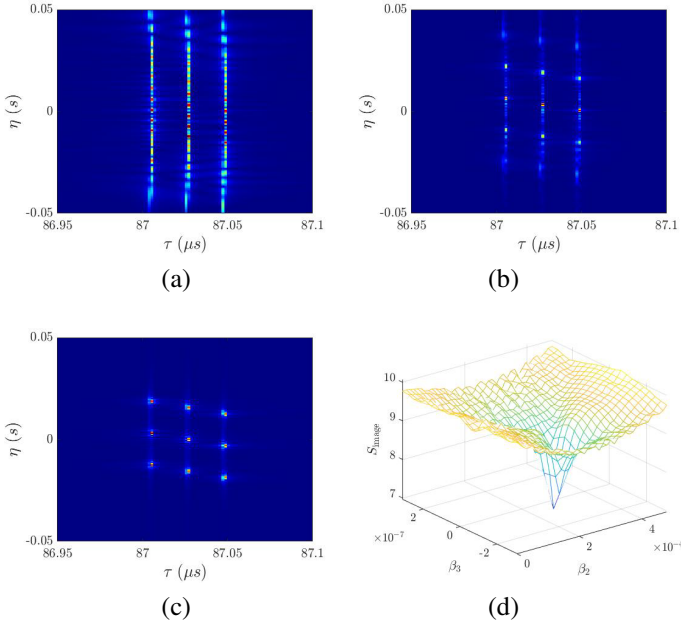


Fig. 6. Magnitude of SAR image with $v_x = 100$ m/s and $\Delta x = \Delta y = 5$ m (a) without autofocus, (b) after applying PGA, (c) after applying MEA, (d) image entropy values under different guesses of (β_2, β_3) .

Fig.6(a) shows the original SAR image with $v_x = 100$ m/s and $\Delta x = \Delta y = 5$ m, without applying autofocus. Similarly, Fig.7(a) shows the original SAR image with same velocity, but $\Delta x = 4$ m, $\Delta y = 10$ m, and Fig.8(a) shows the original SAR image with same velocity and $\Delta x = 10$ m, $\Delta y = 4$ m. In these three images, the scatterers are well focused along range direction since the range compression is accomplished in RDA. However, the point targets are severely blurred along

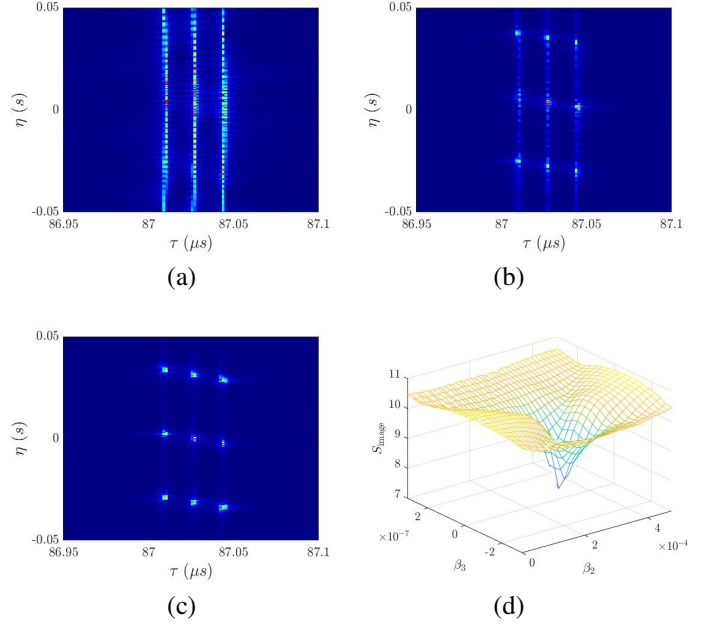


Fig. 7. Magnitude of SAR image with $v_x = 100$ m/s and $\Delta x = 4$ m, $\Delta y = 10$ m (a) without autofocus, (b) after applying PGA, (c) after applying MEA, (d) image entropy values under different guesses of (β_2, β_3) .

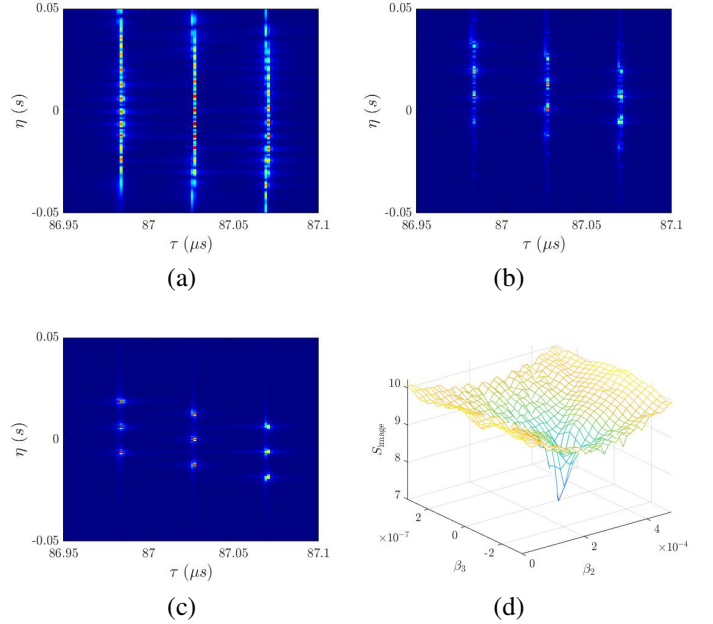


Fig. 8. Magnitude of SAR image with $v_x = 100$ m/s and $\Delta x = 10$ m, $\Delta y = 4$ m (a) without autofocus, (b) after applying PGA, (c) after applying MEA, (d) image entropy values under different guesses of (β_2, β_3) .

azimuth direction. Thus, autofocus is needed to obtain better focused SAR images.

Fig.6(b), Fig.7(b), Fig.8(b) demonstrate the SAR images after autofocused with PGA under three different scenarios, $\Delta x = \Delta y = 5$ m; $\Delta x = 4$ m, $\Delta y = 10$ m; $\Delta x = 10$ m, $\Delta y = 4$ m, respectively. In scenario 1 and 2, the focused SAR images Fig.6(b) and Fig.7(b) are both decently focused, the 9 point targets can be well identified. The targets in Fig.8(b) are not that well-focused, which may be due to the fact that

the spacing along y -direction $\Delta y = 4$ m is relatively small, so the phase error cannot be accurately determined. Also, the positions of the 9 point targets are slightly shifted along azimuth direction, which may result in a misinterpretation on the true positions of point targets. Nevertheless, the 9 point targets in Fig.8(b) can still be distinguished.

Fig.6(c), Fig.7(c), Fig.8(c) show the SAR images after auto-focused with parametric MEA under three different scenarios, $\Delta x = \Delta y = 5$ m; $\Delta x = 4$ m, $\Delta y = 10$ m; $\Delta x = 10$ m, $\Delta y = 4$ m, respectively. In these three figures, all the 9 point targets can be well distinguished after MEA is applied, indicating that the parametric MEA can focus the image well regardless of the target spacings Δx , Δy . It is speculated that for a parametric autofocus method, as long as the correct set of coefficient (β_2, β_3) can be identified, no matter how close the spacings Δx , Δy are, the image can be well focused.

Fig.6(d), Fig.7(d), Fig.8(d) show the change of image entropy under different set of coefficients (β_2, β_3) . The coefficients (β_2, β_3) corresponding to the valley-bottom of these three figures are the correct choice according to minimum entropy criteria. The image entropy of original images, PGA-autofocused images, and MEA-autofocused images are listed in Table I. Thus, it can be concluded that the MEA shows

TABLE I
IMAGE ENTROPY S_{image} OF DIFFERENT SCENARIOS.

scenario	1	2	3
original image	9.908	10.756	10.175
PGA-autofocused	8.407	9.446	8.730
MEA-autofocused	6.968	7.625	7.210

better performance in SAR image focus than PGA, for that the MEA-autofocused images have smaller image entropy than PGA-autofocused images, and the positions of focused targets are not shifted when autofocus is applied.

D. Real SAR Images

The SAR image of a baseball field demonstrated is captured by X-band FARAD SAR in 2015, which is provided by Sandia National Laboratory, U.S. [15]. Assuming this X-band SAR is with same operating parameters as the simulation of 9-point targets in this paper, then we can apply random noises and phase error to the SAR image, and see if the PGA and MEA are able to recover the focused SAR image.

Let the original SAR image be $s_f[m, n]$, the blurred image due to phase error be $s_b[m, n]$, the noisy image be $s_n[m, n]$, and the blurred noisy image be $s_{bn}[m, n]$. In this case, a polynomial phase error is added to $s_f[m, n]$ to obtain $s_b[m, n]$. The phase error is $\varphi(f_\eta) = \beta_2 f_\eta^2 + \beta_3 f_\eta^3$, with $\beta_2 = 2.996 \times 10^{-4}$ and $\beta_3 = -4.876 \times 10^{-7}$. The coefficients are determined such that the image is blurred but there are still some bright scatterers, so that the PGA can work properly. For the scenario with noise presented, the noise is first added to $s_f[m, n]$ to obtain $s_n[m, n]$, then it is blurred with same phase error $\varphi(f_\eta)$ to obtain $s_{bn}[m, n]$. The noise added is the scaled version of additive Gaussian $\mathcal{N}(0, 1)$.

Fig.9(a) shows the original SAR image $s_f[m, n]$. Fig.9(b) demonstrates the blurred SAR image $s_b[m, n]$. Fig.9(c), (d)

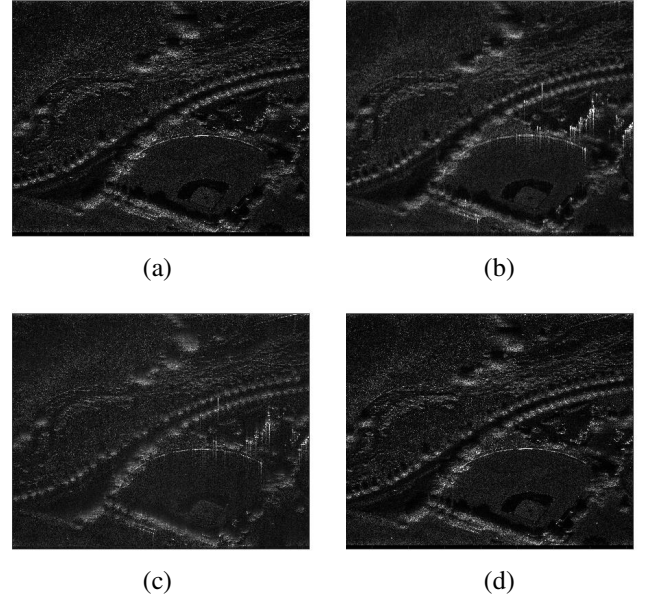


Fig. 9. Magnitude of SAR image (a) $s_f[m, n]$, (b) $s_b[m, n]$, (c) after applying PGA to $s_b[m, n]$, (d) after applying MEA to $s_b[m, n]$.

show the autofocused image by applying PGA, MEA to $s_b[m, n]$, respectively. Both PGA and MEA are effective in autofocusing the real SAR image, as shown in Fig.9(c), (d), but the MEA focuses the image better than PGA, for that Fig.9(d) looks very similar to Fig.9(a).

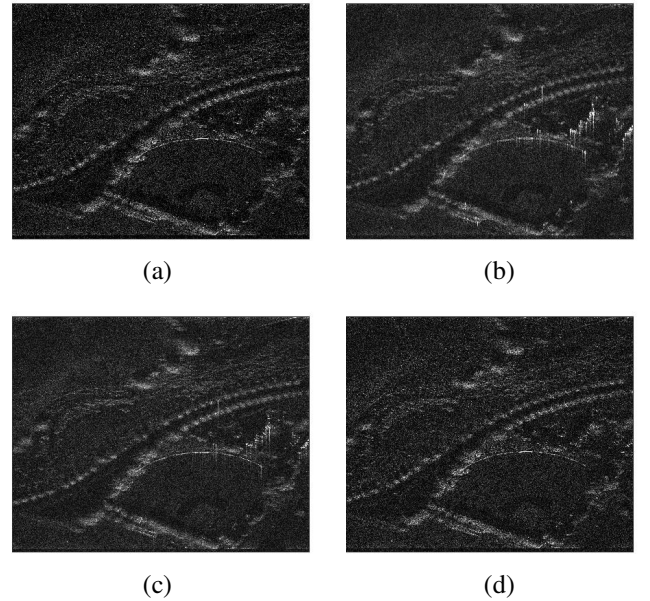


Fig. 10. Magnitude of SAR image (a) $s_n[m, n]$, (b) $s_{bn}[m, n]$, (c) after applying PGA to $s_{bn}[m, n]$, (d) after applying MEA to $s_{bn}[m, n]$.

Fig.10(a) shows the noisy SAR image $s_n[m, n]$. Fig.10(b) demonstrates the blurred noisy SAR image $s_{bn}[m, n]$. Fig.10(c), (d) show the autofocused image by applying PGA, MEA to $s_{bn}[m, n]$, respectively. If the noise is added and the SNR is not too low, both PGA and MEA are able to focus the blurred noisy image. Similarly to the case without noise, the MEA still focuses the image better than PGA, as shown in

Fig.10(c), (d).

The image entropy of blurred images $s_b[m, n]$, PGA-autofocused images, and MEA-autofocused images are listed in Table II. From the figures shown above and the image

TABLE II
IMAGE ENTROPY S_{image} OF DIFFERENT SCENARIOS.

scenario	without noise	with noise
blurred image	22.165	22.653
PGA-autofocused	21.998	22.490
MEA-autofocused	20.720	21.565

entropy listed in Table II, since the MEA-autofocused images are with smaller image entropy, the MEA can focus better than PGA, as long as the correct coefficients can be determined. However, the MEA is also more time consuming, since it is required to calculate the entropy for every given set of coefficients. On the contrary, though the PGA cannot produce better focused image, it is very efficient, as long as there are bright scatterers, the phase error can usually be estimated within 10 iterations. Also, from the results presented in Fig.9(c) and Fig.10(c), the images focused with PGA are still decently focused, which can be seen from the bright scatterers near the baseball field. Most of the blurred bright scatterers in Fig.9(b), Fig.10(b) are focused in Fig.9(c), Fig.10(c), respectively.

It is also worth mentioning that if the phase error is more significant such that there are no bright scatterers, then the PGA may not focus the image well, this is because the center shifting and windowing require obvious bright scatterers so that the phase error estimation would converge after several iteration. Similarly, if the noise is too large, or the SNR is too small, the PGA may not focus the image well, either.

VI. CONCLUSIONS

In this term paper, several SAR autofocus methods including phase gradient autofocus (PGA) and three variants of minimum-entropy autofocus (MEA), are illustrated in details. The parametric MEA with conventional polynomial model and PGA are implemented with Matlab, and the autofocus results are presented in Section V. Both the real SAR image and simulated SAR image of point targets are both used to demonstrate the effectiveness of PGA and MEA.

If the reader is interested in SAR principles and algorithms, the book by Cumming and Wong [1] provides many details. If the reader is interested in SAR autofocus, other methods such as minimum-entropy autofocus with Chebyshev polynomial model [17], contrast optimization [18], [19] and sharpness optimization [5], which are similar to minimum-entropy method but with different evaluation parameter, or the phase-based map-drift method [20], [21] using the concept of autocorrelation, can be further investigated.

REFERENCES

- [1] I. G. Cumming and F. H. Wong, *Digital Processing of Synthetic Aperture Radar Data: Algorithms and Implementation*, 2005.
- [2] J. Wang and X. Liu, "SAR minimum-entropy autofocus using an adaptive-order polynomial model," *IEEE Geoscience and Remote Sensing Letters*, vol. 3, pp. 512-516, Oct. 2006.

- [3] Y. Li and S. O'Young, "Kalman Filter Disciplined Phase Gradient Autofocus for Stripmap SAR," *IEEE Trans. Geosci. Remote Sensing*, vol. 58, no. 9, pp. 6298-6308, Sept. 2020.
- [4] D. E. Wahl, P. H. Eichel, D. C. Ghiglia and C. V. Jakowatz, "Phase gradient autofocus-a robust tool for high resolution SAR phase correction," *IEEE Trans. Aerospace Electronic Systems*, vol. 30, no. 3, pp. 827-835, July 1994.
- [5] R. L. Morrison, M. N. Do and D. C. Munson, "SAR Image Autofocus By Sharpness Optimization: A Theoretical Study," *IEEE Trans. Image Processing*, vol. 16, no. 9, pp. 2309-2321, Sep. 2007.
- [6] P. H. Eichel and C. V. Jakowatz, "Phase-gradient algorithm as an optimal estimator of the phase derivative," *Opt. Lett.*, vol. 14, pp. 1101-1103, Oct. 1989.
- [7] A. Evers and J. A. Jackson, "A Generalized Phase Gradient Autofocus Algorithm," *IEEE Trans. Computational Imaging*, vol. 5, no. 4, pp. 606-619, Dec. 2019.
- [8] C. V. Jakowatz and D. E. Wahl, "Eigenvector method for maximum-likelihood estimation of phase errors in synthetic-aperture-radar imagery," *J. Opt. Soc. Am. A*, vol. 10, pp. 2539-2546, Dec. 1993.
- [9] H. Zeng, W. Yang, P. Wang and J. Chen, "A Modified PGA for Spaceborne SAR Scintillation Compensation Based on the Weighted Maximum Likelihood Estimator and Data Division," *IEEE J. Selected Topics in Applied Earth Observations and Remote Sensing*, vol. 15, pp. 3938-3947, 2022.
- [10] H. J. Callow, M. P. Hayes and P. T. Gough, "Stripmap phase gradient autofocus," in *Oceans 2003. Celebrating the Past ... Teaming Toward the Future*, vol. 5, pp. 2414-2421, 2003.
- [11] D. E. Wahl, C. V. Jakowatz, P. A. Thompson and D. C. Ghiglia, "New approach to strip-map SAR autofocus," in *Proceedings of IEEE 6th Digital Signal Processing Workshop*, pp. 53-56, 1994.
- [12] D. G. Muff, "Electromagnetic Ray-Tracing for the Investigation of Multipath and Vibration Signatures in Radar Imagery," Ph.D. dissertation, Abbrev. Department of Electronic Engineering University College London, London, United Kingdom, Aug. 2018.
- [13] Li Xi, Liu Guosui and Jinlin Ni, "Autofocusing of ISAR images based on entropy minimization," *IEEE Trans. Aerospace Electronic Systems*, vol. 35, no. 4, pp. 1240-1252, Oct. 1999.
- [14] T. Zeng, R. Wang and F. Li, "SAR Image Autofocus Utilizing Minimum-Entropy Criterion," *IEEE Geosci. Remote Sensing Letters*, vol. 10, pp. 1552-1556, Nov. 2013.
- [15] Sandia National Laboratory, "Complex SAR Data, Pathfinder Radar ISR & SAR Systems," *sandia.gov*, 2015. [Online] <http://www.sandia.gov/radar/pathfinder-radar-isr-and-synthetic-aperture-radar-sar-systems/complex-data>. [Accessed Jun. 17, 2022].
- [16] A. Fasih, "Implementation of phase gradient autofocus for SAR images for Matlab," Jun. 21, 2008. [Online] <http://projects.csail.mit.edu/atemuri/wiki/index.php?title=User:Fasih/PGA.m>. [Accessed Jun. 16, 2022].
- [17] T. Xiong, M. Xing, Y. Wang, S. Wang, J. Sheng and L. Guo, "Minimum-Entropy-Based Autofocus Algorithm for SAR Data Using Chebyshev Approximation and Method of Series Reversion, and Its Implementation in a Data Processor," *IEEE Trans. Geosci. Remote Sensing*, vol. 52, pp. 1719-1728, Mar. 2014.
- [18] F. Berizzi and G. Corsini, "Autofocusing of inverse synthetic aperture radar images using contrast optimization," *IEEE Trans. Aerospace and Electronic Systems*, vol. 32, no. 3, pp. 1185-1191, July 1996.
- [19] J. Xu, Y. Peng and X.-G. Xia, "Parametric autofocus of SAR imaging - inherent accuracy limitations and realization," *IEEE Trans. Geosci. Remote Sensing*, vol. 42, no. 11, pp. 2397-2411, Nov. 2004.
- [20] O. O. Bezvesilniy, I. M. Gorovyi and D. M. Vavriv, "Estimation of phase errors in SAR data by Local-Quadratic map-drift autofocus," in *2012 13th International Radar Symposium*, 2012, pp. 376-381.
- [21] L. Zhang, M. Hu, G. Wang and H. Wang, "Range-Dependent Map-Drift Algorithm for Focusing UAV SAR Imagery," *IEEE Geoscience and Remote Sensing Letters*, vol. 13, no. 8, pp. 1158-1162, Aug. 2016.